Competition between Singlet Fission and Spin-Orbit Induced Intersystem Crossing in Anthanthrene and Anthanthrone Derivatives

Youn Jue Bae,[a] Dr. Matthew D. Krzyaniak,[a] Prof. Dr. Marek B. Majewski,[b] Dr. Maude Desroches,[c] Prof. Dr. Jean-François Morin,[c] , Prof. Dr. Yi-Lin Wu,[a],[d] and Prof. Dr. Michael R. Wasielewski[a]*

[a]Department of Chemistry and Institute for Sustainability and Energy at Northwestern, Northwestern University, Evanston IL 60208-3113

[b] Department of Chemistry and Biochemistry and Centre for NanoScience Research, Concordia University, Montréal, Québec, H4B 1R6, Canada

[c] Department of Chemistry, Université Laval, Québec, Québec, G1V 0A6, Canada

[d] Current Address: School of Chemistry, Cardiff University, Main Building, Park Place, Cardiff CF10 3AT, UK

Abstract

Singlet and triplet excited state dynamics of anthanthrene and anthanthrone derivatives in solution are studied. Triisopropylsilyl- (TIPS) or H-terminated ethynyl groups are used to tune the singlet and triplet energies to enable their potential applications in singlet fission and triplet fusion processes. Time-resolved optical and electron paramagnetic resonance (EPR) spectroscopies are used to obtain a mechanistic understanding of triplet formation. The anthanthrene derivatives form triplet states efficiently at a rate (~10^7 s^{-1}) comparable to radiative singlet fluorescence processes with ~30 % triplet yields, despite their large S_1 - T_1 energy gap (> 1 eV) and the lack of carbonyl groups. In contrast, anthanthrone has a higher triplet yield (50 ± 10 %) with a faster intersystem crossing rate (2.7×10^8 s^{-1}) due to the n-π* character of the $S_1 \leftarrow S_0$ transition. Analysis of time-resolved spin-polarized EPR spectra of these compounds reveals that the triplet states are primarily generated by the spin-orbit-induced intersystem crossing mechanism. However, at high concentrations, the EPR spectrum of the 4,6,10,14-tetrakis(TIPS-ethynyl)anthanthrene triplet state shows a significant contribution from a non-Boltzmann population of the $m_s = 0$ spin sublevel, which is characteristic of triplet formation by singlet fission.

1. Introduction

Anthanthrene and anthanthrone chromophores are highly π-conjugated organic molecules with diverse photophysical applications including organic light emitting diodes,[1] dye-sensitized solar cells,[2] and organic field effect transistors.[3] Unlike conjugated polyacenes such as tetracene and pentacene, which are unstable toward light and oxygen due to oxidation,[4] anthanthrene and anthanthrone derivatives are highly stable and chemically tunable.[5] Although the steady-state photophysical properties of anthanthrene-based molecules have been studied extensively,[6] their excited state properties remain underexplored. In order to expand their potential application to singlet fission and triplet fusion, both the singlet and triplet excited decay pathways need to be better understood.

Previous studies of anthanthrene and anthanthrone derivatives have shown that they all undergo spin-orbit-induced intersystem crossing (SO-ISC) with varying triplet yields,[7] where anthanthrone derivatives undergo SO-ISC faster and more efficiently than anthanthrene derivatives. The generation of triplet states in organic molecules has been an interesting topic of research due to the potential leveraging of these excited states to increase photovoltaic device efficiencies.[8] For instance, molecules that can undergo triplet fusion can upconvert near-infrared light to visible wavelengths, whereas molecules that absorb blue light can undergo singlet fission resulting in two triplet states, which can be used to overcome the theoretical Shockley-Queisser efficiency limit for single junction solar cells.[9] Both triplet fusion and fission have been extensively studied in polyacenes.[10] Here, we characterize triplet formation in one anthanthrone and two anthanthrene derivatives (Scheme 1) in solution using time-resolved optical and EPR spectroscopies.

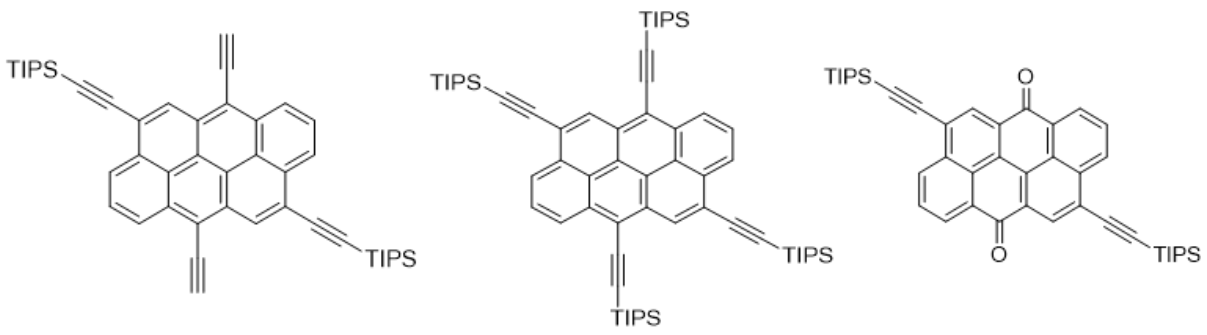

Scheme 1. The anthanthrene (**1** and **2**) and anthanthrone (**3**) derivatives studied here.

2. Results and Discussion

X-ray structural characterization

We report the crystal structures of **2** and **3**, which crystallize into the Pbca and $P2_1/c$ space groups, respectively (Figure 1). Since the anthanthrene core is planar for both molecules there is significant π-conjugation in **1** and **2**. Comparing the packing structure, there is less π- π stacking in **2** than **1** due to steric hindrance from four TIPS groups rather than two. Thus, the crystal structures of these molecules show that the planar aromatic π-system is maintained throughout the series. Detailed information regarding the single crystal structures are given in the Supplementary Information.

Steady-state optical characterization

In order to obtain the S_1 and T_1 energies ($E[S_1]$, and $E[T_1]$), steady-state absorption spectra, as well as fluorescence and phosphorescence emission spectra were collected. The steady-state absorption and emission spectra of **1-3** have well-resolved vibronic progressions, but the linewidth of **3** is significantly broadened (Figure 2). The fluorescence quantum yields of **1-3** (φ_{fl}) are 65 ± 5 %, 55 ± 4 %, and 9 ± 2 %, respectively (Table 1). $E[S_1]$ was determined from the onset of absorption and emission spectra. Comparing $E[S_1]$ among the three molecules, **1** has the highest

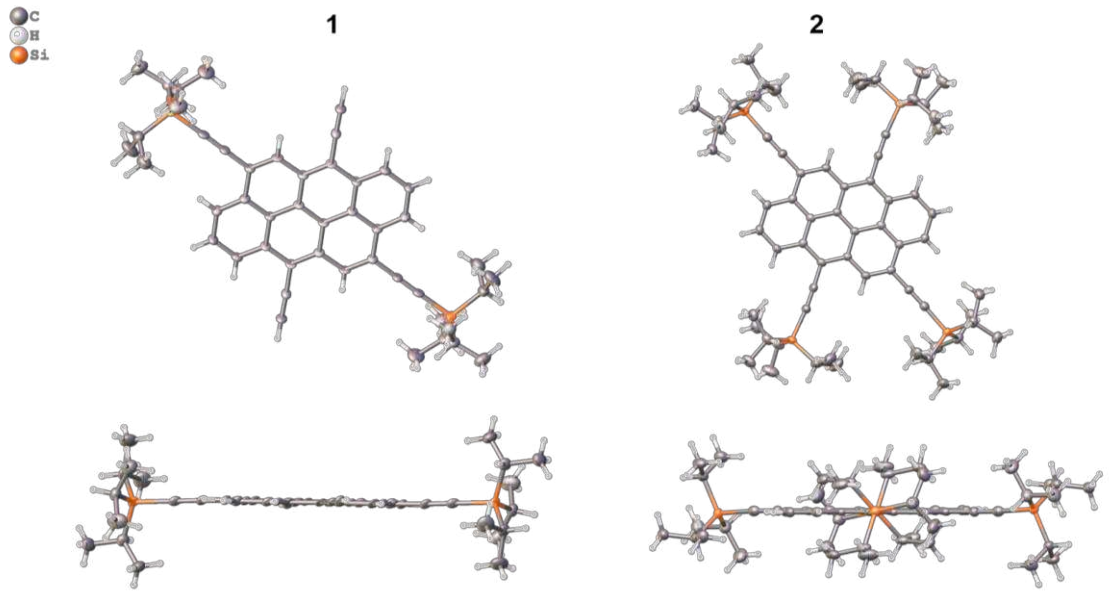

Figure 1. Single crystal structure of molecules **1** and **2**. Grey = carbon atoms; white = hydrogen atoms; orange = silicon atoms.

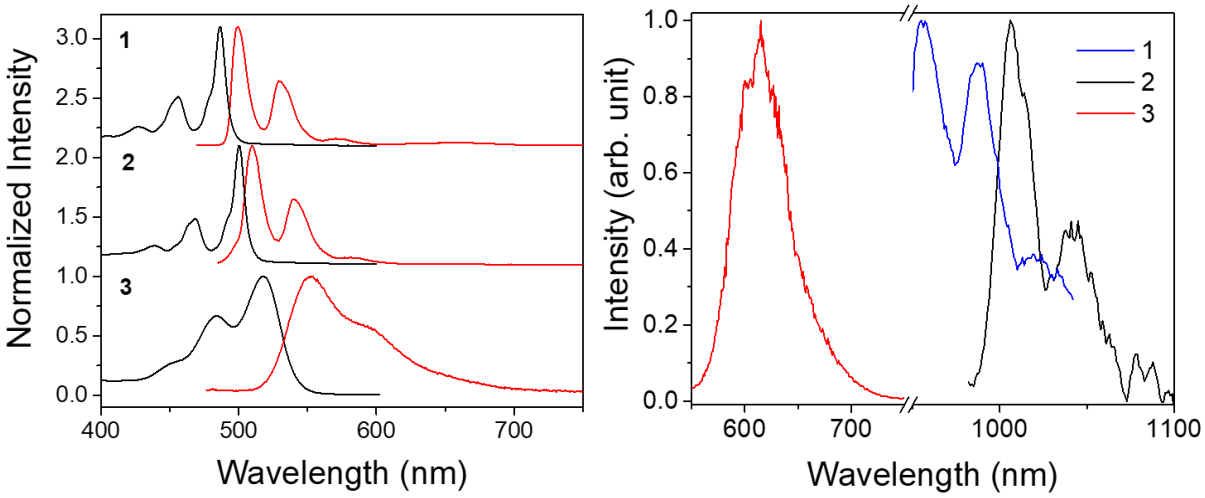

Figure 2. Steady-state absorbance and emission in CH_2Cl_2 (left) and phosphorescence emission of **1** and **2** in 100% iodoethane and **3** in CH_2Cl_2 at 77K (right).

$E[S_1]$ (2.51 eV), followed by **2** (2.46 eV) and **3** (2.25 eV). The maximum of the phosphorescence emission spectrum was used to determine $E[T_1]$. Because **1** and **2** have high fluorescence quantum yields, in order to obtain their phosphorescence spectra, pure iodoethane was used as the solvent

to enhance ISC *via* the heavy atom effect. The phosphorescence emission was collected at 77K and the highest $E[T_1]$ was observed for **3** (2.01 eV) followed by **1** (1.30 eV) and **2** (1.23 eV).

Table 1. Photophysical properties of **1**-**3** in solution.

	λ_{abs} (nm)	λ_{emis} (nm)	φ_{fl} (%)	$E[S_1]$ (eV)	$E[T_1]$ (eV)	$\Delta E([S_1]-[T_1])$ (eV)	φ_{Δ} (%)
1	486	499	65 ± 5	2.51	1.30[a]	1.21	14 ± 3
2	500	510	55 ± 4	2.46	1.23[a]	1.23	20 ± 4
3	518	553	9 ± 2	2.25	2.01	0.24	50 ± 8

[a] Iodoethane is used as the solvent.

Triplet quantum yield

Singlet oxygen ($^1\Delta_g$) emission from the samples in CH_2Cl_2 was measured to quantify their triplet yields (Figure 3). In CH_2Cl_2, molecule **3** has the highest singlet oxygen quantum yield of 50 ± 8 % followed by **2** (20 ± 4%) and **1** (14 ± 3 %). This trend follows the fluorescence quantum yield, where highly fluorescent molecule **1** has the lowest singlet oxygen quantum yield. Since the triplet conversion ($^3\Sigma_g^-$) into singlet oxygen ($^1\Delta_g$) is not quantitative, the singlet oxygen quantum yield gives the lower limit of triplet yield and the fluorescence quantum yield gives the upper limit. The triplet yield range for molecule **1** is 15 - 35%, 20 - 45% for **2** and 50 - 90 % for **3**. Since the phosphorescence and TREPR spectra are obtained in iodoethane, the singlet oxygen quantum yield of **1** and **2** in iodoethane was also measured to be 30 ± 2 % and 40 ± 10 % for molecule **1** and **2**, respectively.

Excited-state dynamics of anthanthrone and anthanthrene derivatives

FsTA spectroscopy was used to examine the singlet and triplet excited state deactivation pathways. At early times, we observed ground state bleach (GSB), stimulated emission (SE) and singlet excited state absorption (ESA) features, while at later times, the SE feature disappears, and spectra indicative of a new species appear (Figure 4). The later time features are assigned to the triplet

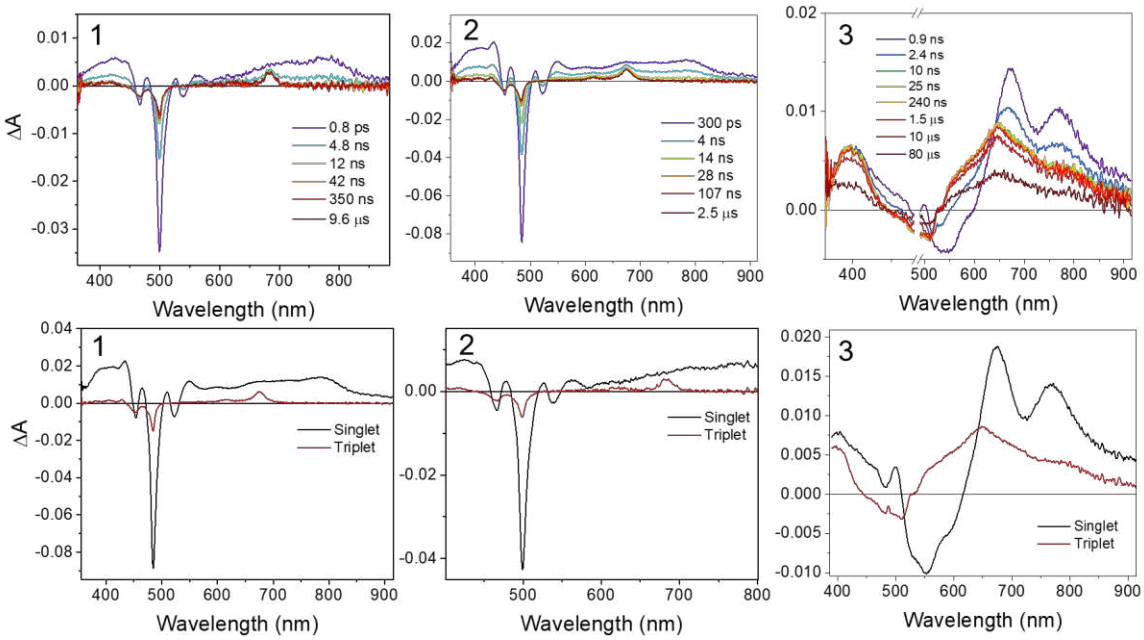

Figure 4. fsTA spectra (top) of **1**-**3** in CH_2Cl_2 and the species-associated spectra (bottom) using the kinetic model A → B → GS. The wavelength fitting and population vs. time plots are shown in Figure S2.

state because we observe singlet oxygen emission and the lifetime of this long-lived species increases when the sample is degassed. Similar to the steady-state absorption and emission spectra, the ESA in **3** is broadened compared to **1** and **2**. This broadened feature is attributed to a contribution from an n ← π^* transition.[7] Compounds **1** and **2** have spectrally well-resolved singlet and triplet features, where the singlet ESA features have a broad absorption from 350 - 900 nm overlapping with the GSB and SE, while the triplet state spectral features occur at 650 nm and 680 nm for **1** and **2**, respectively. Globally fitting the spectra using an A → B → ground state model yields the species-associated spectra, where state A is assigned to S_1, state B is

assigned to T_1. The τ_A is the effective S_1 decay time constant that is composed of radiative decay, internal conversion and intersystem crossing and τ_B is the T_1 lifetime (Table 2). Here, the two-state model is used to allow the population flow between the singlet and triplet. Since we cannot dissect the contributions from the multiple decay pathways in singlet excited state, we obtain the effective time constant τ_A and extrapolate the radiative decay and intersystem crossing rates from the fluorescence and singlet oxygen quantum yield. The population *versus* time and wavelength fits are shown in Figure S2 in the Supporting Information. Compound **3** has the shortest time constant for τ_A (1.8 ± 0.1 ns) followed by **2** (4.0 ± 0.1 ns) and **1** (5.0 ± 0.1 ns), where the trend agrees well with the fluorescence quantum yields. For τ_B **3** has the shortest triplet lifetime (105 ± 1 μs), followed by **1** (185 ± 5 μs) and **2** (440 ± 10 μs). The radiative decay (k_r) and intersystem crossing (k_{isc}) rates can be approximated from the effective singlet decay time constant (τ_A) obtained from the fsTA data, as well as the fluorescence (φ_{fl}) and singlet oxygen quantum yields (φ_Δ), using the following equations:

$$k_r = \frac{1}{\tau_A} \cdot \varphi_{fl} \qquad \text{(eq. 2)}$$

$$k_{isc} = \frac{1}{\tau_A} \cdot \varphi_\Delta \qquad \text{(eq. 3)}$$

Assuming that the triplet yield is equal to singlet oxygen quantum yield, the calculated lower limit for the intersystem crossing rate is given in Table 2.

Table 2. Excited state lifetimes of S_1 and T_1.

	τ_A (ns)	τ_B (μs)	k_r (10^8 s^{-1})	k_{isc} (10^8 s^{-1})
1	5.0 ± 0.1	185 ± 5	1.3 ± 0.1	0.28 ± 0.06
2	4.0 ± 0.1	440 ± 10	1.4 ± 0.1	0.5 ± 0.1
3	1.8 ± 0.1	105 ± 1	0.5 ± 0.1	2.7 ± 0.4

TREPR spectroscopy studies of the intersystem crossing mechanism

TREPR data were collected to identify the mechanism of triplet state formation. Following photoexcitation at 85K in frozen iodoethane and toluene, compound **1** shows a 4-line, spin-polarized TREPR spectrum that is indicative of an axially symmetric electron distribution in T_1 with an (*e,a,e,a*) pattern, where *a* = enhanced absorption and *e* = emission from low to high field (Figure 5).

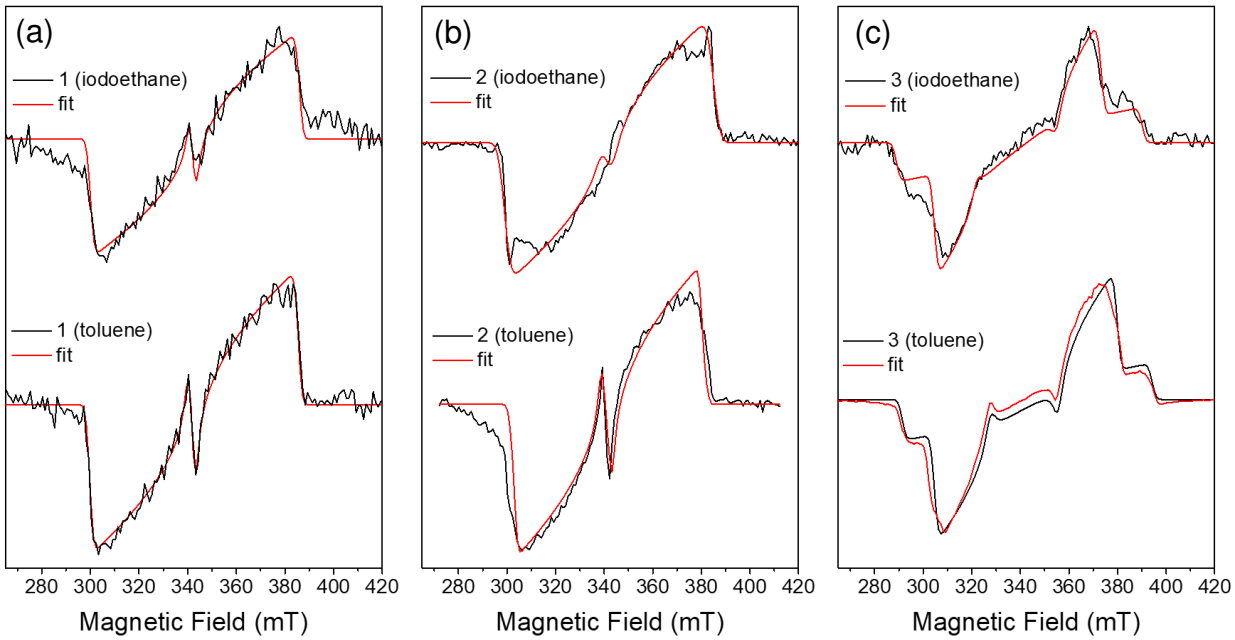

Figure 5. TREPR spectra at 9.5 GHz and 85 K of the triplet states of (a) **1** (λ_{ex}= 495 nm), (b) **2** (λ_{ex}= 485 nm) and (c) **3** (λ_{ex} = 520 nm) in iodoethane (top) and in toluene (bottom).

Simulation of the spectrum shows that the triplet zero-field states T_x, T_y and T_z are populated via SO-ISC with relative rates of P_x:P_y:P_z = 0.14:0.48:0.38 in iodoethane and P_x:P_y:P_z = 0.20:0.45:0.38 in toluene (Table 3). Compound **3** has a 6-line TREPR spectrum spin-polarized TREPR spectrum characteristic of an electron distribution in T_1 having rhombic symmetry with a dominant (*e,e,e,a,a,a*) polarization pattern, where T_1 populated via SO-ISC with relative rates of P_x:P_y:P_z =0.23:0.77:0 in iodoethane and Px:Py:Pz = 0.14:0.83:0.03 in toluene. In contrast, the TREPR

spectrum of **2** has a different polarization pattern in toluene versus iodoethane. In toluene, the triplet zero-field states T_x, T_y and T_z are populated via SO-ISC with relative rates of P_x:P_y:P_z = 0:0.77:0.23 similar to compound **1** in toluene; in iodoethane, however, there is additional sharp features at the low and high field edges, which cannot be fit using the SO-ISC mechanism alone (Figure 5b). For example, the fit shown in Figure 5b assumes that only SO-ISC occurs, and yields an axially symmetric spectrum with an (*e,a,e,a*) polarization pattern and relative populations rates of P_x:P_y:P_z = 0.23:0:0.77; however, the deficiencies in the fit are apparent at 310 and 380 mT along with the center feature.

Table 3. ZFS parameters (|D| and |E|) and relative population rates P_{xyz}.

	|D| (MHz)	|E| (MHz)	|E|/|D|	P_x	P_y	P_z
1[a]	1215	397	0.32	0.14	0.48	0.38
1[b]	1215	397	0.32	0.20	0.45	0.35
2[a]	1233	380	0.31	0.11	0.89	0
2[b]	1240	360	0.29	0	0.77	0.23
2[c]	1080	249	0.23	-	-	-
3[a]	1416	167	0.12	0.23	0.77	0
3[b]	1440	221	0.15	0.14	0.83	0.03

The compound is in [a] iodoethane and [b] toluene. [c] SF-ISC parameters in compound **2**.

It has been shown previously in both polyacenes and terrylenediiimides that singlet exciton fission can result in formation of an initial spin-correlated triplet pair state $^1(T_1T_1)$ that can intersystem cross to first give a quintet spin state $^5(T_1T_1)$, which can then separate to form two T_1 states.[11] The quintet state is formed with its $m_s = 0$ sublevel greatly overpopulated, so that this initial non-Boltzmann spin population is carried over to the $m_s = 0$ sublevel of the T_1 states. As a

consequence, the resulting TREPR spectrum of T_1 has the same (*a,e,e,a,a,e*) spin polarization as is typically observed for the radical-pair intersystem crossing mechanism.[12] We will label this mechanism singlet fission intersystem crossing (SF-ISC). Figure 6 shows that the T_1 spectrum of **2** is best simulated with a linear combination of SF-ISC (47%) and SO-ISC (53%). Since the concentration of **2** for the TREPR experiments is high, presumably some small aggregates form in the frozen solvent matrix, which undergo singlet fission resulting in the $m_s = 0$ populated triplet states.

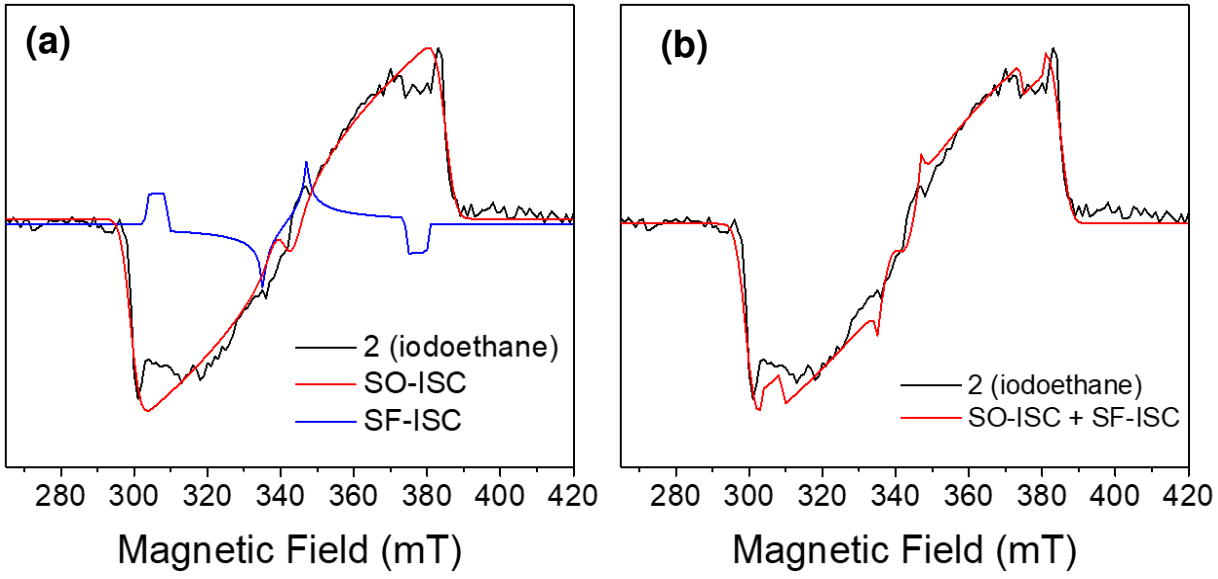

Figure 6. TREPR spectral fitting using (a) SO-ISC and SF-ISC and (b) linear combination of 53% SO-ISC and 47% SF-ISC.

Although the concentrations of **2** in toluene and in iodoethane are same, the SF-ISC feature is only observed in iodoethane. Since the heavy atom effect in iodoethane does not change the triplet polarization pattern in compounds **1** and **3**, we attribute the appearance of the SF-ISC triplet in compound **2** to a change in the electronic coupling among the aggregated molecules of **2**. Aggregation of **2** in solution is indicated by the change in vibronic peak ratio in its steady state

absorption spectrum (Figure S4). In addition, the difference in $|D|$ and $|E|$ values between SO-ISC and SF-ISC triplets (Table 3) indicates different types of aggregate formation in toluene *versus* iodoethane. It has been shown that $|D|$ and $|E|$ values are different between herringbone and parallel orientations of dilute pentacene films due to a change in the dipolar coupling.[13] The smaller $|D|$ value of compound **2** in iodoethane indicates that the electron distribution in the triplet state is more delocalized in the aggregate formed in iodoethane than it is in toluene. On the other hand, triplet spectrum of **1** in frozen iodoethane can be fit exclusively using the SO-ISC mechanism indicating that aggregates favorable for singlet fission may not form upon cooling solutions of **1** to 85K, or if they do form, either their geometry or energetics are inadequate for singlet fission.

Comparison of experimental and computed excited state energies

In order to understand the S_1 and T_1 energy trends, TDDFT calculations were performed and the results are listed in Table 4.

Table 4. Comparison of Experimental and Computed (TDDFT) values of $E[S_1]$ and $E[T_1]$

	$E[S_1]$ (eV)	$\Delta E([S_1]_{exp}\text{-}[S_1]_{calc})$	$E[T_1]$ (eV)	$\Delta E([T_1]_{exp}\text{-}[T_1]_{calc})$
1	2.45	0.06	1.08	0.22
2	2.37	0.09	1.05	0.18
3	2.62	-0.37	1.56	0.45

Comparing the $E[S_1]$ and $E[T_1]$ values of the derivatives studied here to previously reported anthanthrene and anthanthrone derivatives,[7] which have phenyl and *t*-butylphenyl groups at the 4-, 6-, 10- and 12-positions, $E[S_1]$ and $E[T_1]$ are lower in molecules **1-3**; however, molecules **1** and **2** have a greater S_1-T_1 energy gap relative to previously studied anthanthrene derivatives. Such energetics are desirable for potential applications including singlet fission and/or fusion. For

instance, **1** and **2** absorb strongly in the blue region of the visible spectrum and twice the triplet energy is slightly uphill for **1** by only 0.09 eV, S_1 and $2 \times T_1$ are nearly isoenergetic for **2**. Tetracene and perylenediimide systems undergo near quantitative singlet fission despite the fact that this process is endoergic by about 0.2 eV.[10b, 14]

Comparing the singlet excited state dynamics in the molecules studied here to the previously reported anthanthrenes, both **1** and **2** are highly fluorescent similar to phenyl and *p*-(*t*-butylphenyl substituted anthanthrene derivatives.[7] Fluorescence is the major deactivation pathway in **1** and **2**; however, **3** has a low fluorescence quantum yield because SO-ISC is competitive with fluorescence decay. Compound **3** has an order of magnitude faster SO-ISC rate compared to **1** and **2**. The smaller S_1-T_1 energy gap (0.24 eV) allows for efficient SO-ISC in **3**. Although the energy gap in **2** is greater than in **1**, SO-ISC is almost twice as efficient in **2** relative to **1**. This could be due to having greater spin-orbit coupling in **2** compared to **1** because there are four TIPS groups; however, as shown in Figure 6, it is more likely that some of the singlet excited state population of **2** may undergo singlet fission, which is a spin-allowed process, to enhance the triplet formation yield.

3. Conclusion

We were able to tune the singlet and triplet energies of anthanthrene and anthanthrone derivatives by the addition of TIPS and ethynyl groups at the 4-,6-,10- and 12-positions. Compound **3** has the largest SO-ISC rate and highest triplet yield, followed by **2** and **1**. Since **3** has the smallest S_1-T_1 energy gap, SO-ISC is significantly enhanced. Although, **1** has a smaller S_1-T_1 energy gap than **2**, the latter undergoes faster ISC attributed to a small population of singlet excitons undergoing singlet fission based on the triplet polarization pattern observed in its TREPR

spectrum. Based on the work shown here, derivatives based on **1** and **2** are promising molecules for singlet fission and/or fusion applications.

4. Experimental Section

Synthesis

Compounds **1-3** were synthesized using previously reported procedures.[5, 15]

Single crystal structure and x-ray spectroscopy

Crystals of **1** and **2** were grown by slow solvent evaporation of each compound from chloroform solution. The crystals were mounted on a polymer loop with Paratone oil, and the data were collected at 100 K on a Bruker Kappa APEX II CCD diffractometer equipped with a Cu Kα 1 μS microfocus source for crystal **1** and Mo Kα 1 μS for crystal **2** with MX optics. The data were absorption-corrected using SADABS. The structure was solved using SHELXT and refined using SHELXL using Olex 2 software.[16] The structures have been deposited in the Cambridge Crystallographic Data Centre database **1:** CCDC number for **1** is 1937383 and for **2** is 1937384 (Table S1).

Steady-state spectroscopy

Steady-state absorption spectra of the solution samples were measured using a Shimadzu UV-1800 spectrometer and steady-state fluorescence spectra were measured in the front-face mode with a HORIBA Nanolog spectrofluorimeter equipped with an integrating sphere (Horiba Quanta - φ) for absolute fluorescence quantum yield determination. Steady-state fluorescence spectra were collected using CCD detector at 295K and phosphorescence spectra are collected using InP/InGaAs detector at 77K.

Singlet oxygen measurement

The singlet oxygen ($^1\Delta_g$) quantum yield (φ_Δ) was measured using zinc *meso*-tetraphenylporphyrin (ZnTPP) in CH_2Cl_2 as the standard (φ_Δ = 0.7).[17] The absorbance of the sample and the standard is matched to within 0.1 at the excitation wavelength (λ_{ex}) of 435 nm. The singlet oxygen emission spectrum was integrated from λ_1 = 1230 nm to λ_2 =1330 nm, and φ_Δ of the sample was determined using the following equation:[18]

$$\varphi_\Delta\,(\text{sample}) = \varphi_\Delta(\text{ZnTPP}) \cdot \frac{\text{ZnTPP OD at } \lambda_{ex}}{\text{sample OD at } \lambda_{ex}} \cdot \frac{\int_{\lambda_1}^{\lambda_2} I_{sample}(\lambda)\, d\lambda}{\int_{\lambda_1}^{\lambda_2} I_{ZnTPP}(\lambda)\, d\lambda} \qquad (\text{eq. } 1)$$

Transient absorption spectroscopy and global analysis

Femtosecond transient absorption spectroscopy (fsTA) was performed using a regeneratively amplified Ti:sapphire laser system operating at 1kHz to generate 828 nm. The frequency-doubled 414 nm light is used to pump a lab built optical parametric amplifier to generate tunable pump wavelengths of 495 nm, 500 nm and 580 nm for **1**, **2**, and **3** respectively.[19] Solution samples were prepared in 2 mm path length glass cuvettes and degassed with three freeze-pump-thaw cycles. The TA data were subjected to global kinetic analysis to obtain the evolution- and decay-associated spectra and kinetic parameters as described in detail previously.[20]

Time-resolved electron paramagnetic resonance (TREPR) spectroscopy

X-band (~9.6 GHz) measurements were made using a Bruker Elexsys E680-X/W EPR spectrometer outfitted with a split-ring resonator (ER4118X-MS3). TREPR spectra of **1** - **3** were acquired in iodoethane and toluene at 85 K following photoexcitation with a 7 ns (3 mJ/pulse) laser pulse generated by an optical parametric oscillator (Spectra-Physics Basi-scan), pumped with the output of a frequency-tripled Nd-YAG laser (Spectra-Physics Quanta-Ray LAB-170). The kinetic traces of the transient magnetization were acquired in quadrature under continuous

microwave irradiation (5 mW). The EPR spectra were processed in MATLAB and the spectral simulations were performed using EasySpin.[21]

Computational detail (TDDFT)

The ground-state geometry was optimized using QChem (version 5.0) using DFT and TDDFT at B3LYP/6-31G* level. The excited-state energy was calculated using the ground state geometry in vacuum.

5. Keywords

Anthanthrone, Anthanthrene, Excitons, Singlet Fission, Spin-Orbit Intersystem Crossing

6. Acknowledgement

This work was supported by the U.S. Department of Energy, Office of Science, Office of Basic Energy Sciences under Award DE-FG02-99ER14999 (M.R.W.). This work made use of the IMSERC at Northwestern University, which has received support from the Soft and Hybrid Nanotechnology Experimental (SHyNE) Resource (NSF ECCS-1542205), the State of Illinois, and the International Institute for Nanotechnology (IIN). Y.B. thanks Charlotte Stern for helpful discussions regarding X-ray work. M.B.M. acknowledges support from the Natural Sciences and Engineering Research Council of Canada and Fonds de recherche du Québec – Nature et technologies.

7. References

[1] B. K. Shah, D. C. Neckers, J. Shi, E. W. Forsythe, D. Morton, *J. Phys. Chem. A* **2005**, *109*, 7677-7681.

[2] aY. Geng, C. Yi, M. P. Bircher, S. Decurtins, M. Cascella, M. Grätzel, S.-X. Liu, *RSC Advances* **2015**, *5*, 98643-98652; bL. Zhang, B. Walker, F. Liu, N. S. Colella, S. C. B.

Mannsfeld, J. J. Watkins, T.-Q. Nguyen, A. L. Briseno, *J. Mater. Chem.* **2012**, *22*, 4266-4268.

[3] aJ.-B. Giguère, N. S. Sariciftci, J.-F. Morin, *J. Mater. Chem. C* **2015**, *3*, 601-606; bL. Zhang, A. Fonari, Y. Zhang, G. Zhao, V. Coropceanu, W. Hu, S. Parkin, J.-L. Brédas, A. L. Briseno, *Chem. Eur. J.* **2013**, *19*, 17907-17916.

[4] W. Fudickar, T. Linker, *J. Am. Chem. Soc.* **2012**, *134*, 15071-15082.

[5] J.-B. Giguère, J. Boismenu-Lavoie, J.-F. Morin, *J. Org. Chem.* **2014**, *79*, 2404-2418.

[6] B. K. Shah, D. C. Neckers, J. Shi, E. W. Forsythe, D. Morton, *Chem. Mater.* **2006**, *18*, 603-608.

[7] D. J. Stewart, J. Shi, T. R. Naranjo, T. A. Grusenmeyer, J. M. Artz, C. L. McCleese, R. M. O'Donnell, T. M. Cooper, W. M. Shensky, J. E. Haley, *Phys. Chem. Chem. Phys.* **2018**, *20*, 28412-28418.

[8] M. C. Hanna, A. J. Nozik, *J. Appl. Phys.* **2006**, *100*, 074510.

[9] W. Shockley, H. J. Queisser, *J. Appl. Phys.* **1961**, *32*, 510-519.

[10] aS. Singh, W. J. Jones, W. Siebrand, B. P. Stoicheff, W. G. Schneider, *J. Chem. Phys.* **1965**, *42*, 330-342; bJ. J. Burdett, A. M. Müller, D. Gosztola, C. J. Bardeen, *J. Chem. Phys.* **2010**, *133*, 144506; cY. J. Bae, G. Kang, C. D. Malliakas, J. N. Nelson, J. Zhou, R. M. Young, Y. L. Wu, R. P. Van Duyne, G. C. Schatz, M. R. Wasielewski, *J. Am. Chem. Soc.* **2018**, *140*, 15140-15144; dH. Marciniak, M. Fiebig, M. Huth, S. Schiefer, B. Nickel, F. Selmaier, S. Lochbrunner, *Phys. Rev. Lett.* **2007**, *99*, 176402.

[11] aS. L. Bayliss, L. R. Weiss, A. Rao, R. H. Friend, A. D. Chepelianskii, N. C. Greenham, *Phys. Rev. B* **2016**, *94*, 045204; bL. R. Weiss, S. L. Bayliss, F. Kraffert, K. J. Thorley, J. E. Anthony, R. Bittl, R. H. Friend, A. Rao, N. C. Greenham, J. Behrends, *Nat. Phys.*

2017, *13*, 176-181; cM. J. Y. Tayebjee, S. N. Sanders, E. Kumarasamy, L. M. Campos, M. Y. Sfeir, D. R. McCamey, *Nat. Phys.* **2017**, *13*, 182-188; dB. S. Basel, J. Zirzlmeier, C. Hetzer, B. T. Phelan, M. D. Krzyaniak, S. R. Reddy, P. B. Coto, N. E. Horwitz, R. M. Young, F. J. White, F. Hampel, T. Clark, M. Thoss, R. R. Tykwinski, M. R. Wasielewski, D. M. Guldi, *Nat. Commun.* **2017**, *8*, 15171; eM. Chen, M. D. Krzyaniak, J. N. Nelson, Y. J. Bae, S. M. Harvey, R. D. Schaller, R. M. Young, M. R. Wasielewski, *Proc. Natl. Acad. Sci. U. S. A.* **2019**, *116*, 8178-8183.

[12] Z. E. X. Dance, M. J. Ahrens, A. M. Vega, A. B. Ricks, D. W. McCamant, M. A. Ratner, M. R. Wasielewski, *J. Am. Chem. Soc.* **2008**, *130*, 830-832.

[13] D. Lubert-Perquel, E. Salvadori, M. Dyson, P. N. Stavrinou, R. Montis, H. Nagashima, Y. Kobori, S. Heutz, C. W. M. Kay, *Nat. Commun.* **2018**, *9*, 4222.

[14] S. W. Eaton, L. E. Shoer, S. D. Karlen, S. M. Dyar, E. A. Margulies, B. S. Veldkamp, C. Ramanan, D. A. Hartzler, S. Savikhin, T. J. Marks, M. R. Wasielewski, *J. Am. Chem. Soc.* **2013**, *135*, 14701-14712.

[15] J.-B. Giguère, Q. Verolet, J.-F. Morin, *Chem. Eur. J.* **2013**, *19*, 372-381.

[16] O. V. Dolomanov, L. J. Bourhis, R. J. Gildea, J. A. K. Howard, H. Puschmann, *J. Appl. Crystallogr.* **2009**, *42*, 339-341.

[17] R. W. Redmond, J. N. Gamlin, *Photochem. Photobiol.* **1999**, *70*, 391-475.

[18] N. Epelde-Elezcano, E. Palao, H. Manzano, A. Prieto-Castañeda, A. R. Agarrabeitia, A. Tabero, A. Villanueva, S. de la Moya, Í. López-Arbeloa, V. Martínez-Martínez, M. J. Ortiz, *Chem. Eur. J.* **2017**, *23*, 4837-4848.

[19] S. R. Greenfield, M. R. Wasielewski, *Opt. Lett.* **1995**, *20*, 1394-1396.

[20] R. M. Young, S. C. Jensen, K. Edme, Y. Wu, M. D. Krzyaniak, N. A. Vermeulen, E. J. Dale, J. F. Stoddart, E. A. Weiss, M. R. Wasielewski, D. T. Co, *J. Am. Chem. Soc.* **2016**, *138*, 6163-6170.

[21] S. Stoll, A. Schweiger, *J. Magn. Reson.* **2006**, *178*, 42-55.

Graphical Abstract

The intersystem crossing mechanism of anthanthrene and anthanthrone compounds is investigated. Favorable energetics for singlet fission, ($2 \times E[T_1] = E[S_1]$) following photoexcitation of tetrakis(TIPS-ethynyl)anthanthrene allows triplet state formation via singlet fission to compete effectively with spin-orbit-induced intersystem crossing.